

# Ablation model for semiconductors and dielectrics under ultrafast laser pulses for solar cells micromachining

Alberto Gurizzan and Paolo Villoresi<sup>a</sup>

Polo Fotovoltaico Veneto, Dipartimento di Ingegneria dell'Informazione, Università degli Studi di Padova, Via Gradenigo 6, 35131 Padova, Italy

Received: 22 September 2014 / Revised: 19 December 2014

Published online: 30 January 2015 – © Società Italiana di Fisica / Springer-Verlag 2015

**Abstract.** Ultrafast laser pulses provide a new tool for material processing. The ultrafast regime leads to nonlinear absorption and nonthermal interaction with the target yielding significant advantages in solar cells micromachining over traditional mechanical or Q-switched laser processes: high process speed, high energetic efficiency, reduced heat affected zone (HAZ), high quality and precision of the realized structures. Therefore, a description of the dominant physical processes underlying the ultrafast laser-matter interaction is needed to develop a simplified model able to provide an explanation of the different aspect of the process. This paper provides an overview of the fundamental equations governing the laser-material interaction process in a typical dielectric-semiconductor structure and discusses the solution on a 3D axisymmetric domain obtained with a finite element method (FEM) software applied to the problem of selective dielectric delamination in PV solar cells.

## 1 Introduction

In the fabrication of a silicon PV solar cell, several steps involve direct material ablation. For example, the active area of the cell must be isolated from the edges to prevent shunting of the junction itself, which accounts for the 15% of the total loss mechanism [1]. To do so, a groove following the perimeter of the cell is scribed completely through the *n*-type layer, which depth is in the order of few microns. The quality of the groove in terms of shape factor (which impacts on the total cell shading, *i.e.* the fraction of active area lost) and the minimization of the damage to the surrounding structures are then crucial to achieve the maximum cell efficiency.

Another issue is the realization of openings in the dielectric layer on PERC (passivated emitter rear cell) type cells, either on the front or the back, to allow the formation of the metal contacts. The aim here is to selectively remove the dielectric layer without damaging the semiconductor beneath. It has been proven that it is possible to use sub-picosecond pulses with photon energies above the silicon bandgap to selectively delaminate the dielectric layer without noticeable damage to the opened surface [2]. Currently different opening patterns are being studied for the optimal trade-off between surface passivation and resulting contact series resistance [3].

Recently, aside the conventional chemical etching techniques, ablation techniques involving laser pulses are being utilized, such as nanosecond Q-switched pulsed laser. However it is only with the development of chirped pulse amplification (CPA), which led up to commercially available femtosecond laser systems in the mJ pulse energy range, that ultrashort pulses are being investigated for solar cell industrial micromachining.

In ablation with pulsed laser radiation, depending on the respective pulse length range, different beam-matter interaction mechanisms become dominant. As compared in fig. 1, for longer laser pulses in the micro- and nanosecond regime the ablation process is dominated by heat conduction, melting and evaporation. Because the pulse duration and heat conduction are roughly in the same timescale, there is significant time for heat conduction to occur before the pulse ends. Energy of the laser pulse is absorbed on the surface of the workpiece and heat conduction leads to the formation of a temperature field. Depending on the achieved temperature the material is molten or evaporates. Ablation is determined by both evaporation and melt expulsion. An approach that instead of direct laser ablation exploits the temperature-induced stress field to induce the scribing of the semiconductor layer on thin film CIGS solar cells was demonstrated in [4].

<sup>a</sup> e-mail: paolo.villoresi@dei.unipd.it

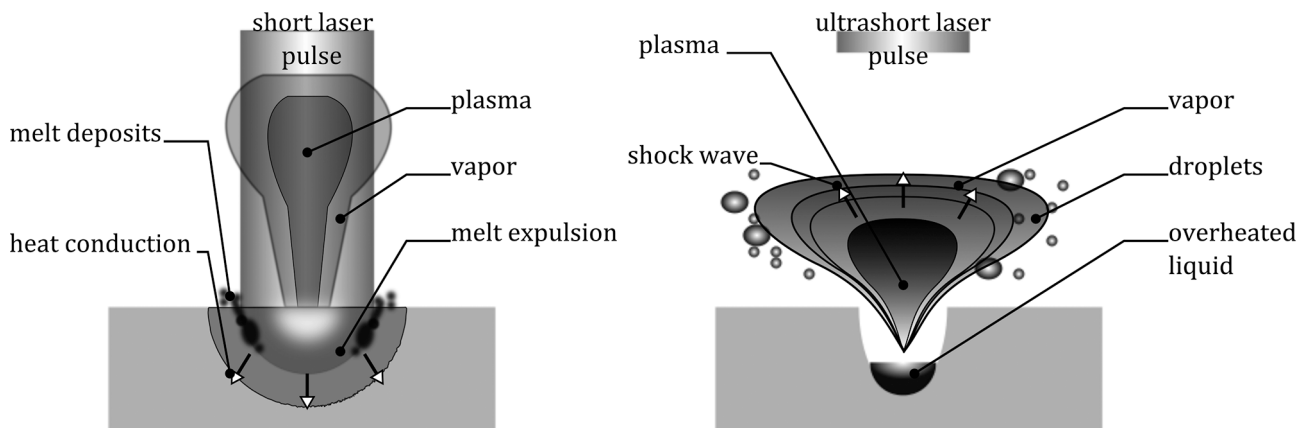


**Fig. 1.** Laser-target interaction. Left: short pulse regime; right: ultrashort pulse regime.

For ultrashort pico- and femtosecond laser pulses and the thereby related short timescales, these classical descriptions of beam-matter interaction lose their validity. Due to the high intensity of ultrashort laser pulses, the absorption is increased by nonlinear multi-photon absorption processes and by the high density free electron plasma that is produced. Furthermore, within pico- and femtosecond timescales the energy transfer from the electron gas to the lattice is not possible. Hence the need for a different thermal description that distinguishes between electron and lattice temperature: the two-temperature model (TTM) [5, 6]. In ultrashort pulse laser ablation extreme pressures, densities and temperatures build up and accelerate the ionized material to high velocities. Due to the short interaction time the material cannot evaporate continuously but is transferred into a state of overheated liquid. This merges into a high pressure mixture of liquid droplets and vapor expanding rapidly, leading to ablation.

## 2 Fundamental equations

Following the approach developed in [7] and [8], the change in the optical properties of the excited material due to the presence of a free electron gas can be described in the Drude approximation with a complex dielectric function:

$$\epsilon = \epsilon_m - \frac{n_e}{n_{cr}} \frac{1}{1 + i/(\omega\tau_D)}, \quad (1)$$

where  $\omega$  is the laser frequency,  $\epsilon_m$  is the unexcited material dielectric function,  $\tau_D$  is the Drude damping time and  $n_e$  is the number of photogenerated electrons. At the critical electron density

$$n_{cr} = \epsilon_0 m_e \omega^2 / e^2 \quad (2)$$

the plasma becomes strongly absorbing and the reflectivity increases.  $e$  and  $m_e$  are, respectively, the electron charge and mass,  $\epsilon_0$  is the vacuum permittivity. If  $\lambda$  is the laser wavelength, then the absorption coefficient of the excited material can be written as

$$\alpha_{fca} = \frac{4\pi}{\lambda} \text{Im} [\sqrt{\epsilon}]. \quad (3)$$

### 2.1 Free electrons plasma

The first step is to describe how radiation interacts with the electronic system of the target. In addition to the classical linear ionization, described by a constant ionization coefficient  $\sigma_0$ , when the intensity is sufficiently high ( $10^{12}$ – $10^{13}$  W/cm<sup>2</sup>), the ionization coefficient becomes intensity dependent because of the simultaneous absorption of multiple photons (MPI) by valence electrons. MPI becomes the dominant process, especially in dielectrics materials, where typically a single photon in the visible spectrum has insufficient energy to promote a conduction band electron. Once the valence band electrons have absorbed enough energy to overcome the material bandgap  $E_g$ , they can freely absorb further energy from the electric field, eventually gaining enough kinetic energy to ionize by impact another atom. This process, which has exponential growth, is called avalanche ionization (AI) [9]. In dense plasmas the recombination proceeds mainly by three-body collisions with one electron acting as a third body: in semiconductors Auger recombination is considered, while in dielectrics only SRH recombination through trap states is considered [10, 11].

**Table 1.** Model constants.

Aluminum oxide			Silicon		
Symbol	Expression	Unit	Symbol	Expression	Unit
$E_g$	9	eV	$E_g$	1.12	eV
$\sigma_m$	$8 \times 10^9$ (with $m = 6$ )	$\text{cm}^{-3}/\text{ps}(\text{cm}^2/\text{TW})^6$	$\sigma_0$	1021	$\text{cm}^{-1}$
$\alpha$	6	$\text{cm}^2/\text{J}$	$\sigma_m$	10 (with $m = 2$ )	$\text{cm}/\text{GW}$
$\epsilon_g$	3.098		$\delta$	$3.6 \times 10^{10} \exp(-1.5E_g/k_b T_e)$	$\text{s}^{-1}$
$\tau_r$	1	ps	$\epsilon_g$	$13.46 + i0.028$	
$T_c$	4950	K	$C$	$3.8 \times 10^{-31}$	$\text{cm}^6/\text{s}$
$\rho_c$	0.89	$\text{g}/\text{cm}^3$	$\tau_0$	$6 \times 10^{-12}$	s
			$\tau_r$	$240 \times 10^{-15}(1 + (n_e/n_{cr})^2)$	s
			$T_c$	7925	K
			$\rho_c$	0.76	$\text{g}/\text{cm}^3$

The equation governing the electron plasma formation takes the form of a rate equation for the free electron density  $n_e$ :

$$\frac{\partial n_e}{\partial t} = \left[ \left( \sigma_0 + \sigma_m \frac{I^{m-1}}{m} \right) \frac{I}{h\nu} + \delta n_e \right] \frac{N_a - n_e}{N_a} - \frac{n_e}{\tau_0 + \frac{1}{C n_e^2}} \quad \text{Semiconductors,} \quad (4a)$$

$$\frac{\partial n_e}{\partial t} = \left[ \sigma_m \frac{I^m}{m} + \alpha I n_e \right] \frac{N_a - n_e}{N_a} - \frac{n_e}{\tau_r} \quad \text{Dielectrics,} \quad (4b)$$

where  $\sigma_m$  is the multi-photon (with  $m$  photons) ionization cross section;  $I$  is the laser intensity;  $N_a$  is the number of nonionized atoms;  $h$  is the Planck constant and  $\nu$  is the laser frequency. The other parameters are listed in table 1. In the present model we neglect the effect on the density rate due to tunnel ionization, by considering that its action is relevant for a regime in pulse intensity higher than the one considered here.

## 2.2 Nonlinear propagation

Describing the beam as a plane wave in the proximity of the focal plane allows us to write a Lambert-Beer type of absorption equation with the time-dependent absorption coefficient  $\alpha_{fca}$  which accounts for the absorption of the electron gas.

$$\frac{\partial I}{\partial z} = - \left[ \frac{N_a - n_e}{N_a} (\sigma_0 + \sigma_m I^{m-1}) + \alpha_{fca} \right] I \quad \text{Semiconductors,} \quad (5a)$$

$$\frac{\partial I}{\partial z} = - \left[ \frac{N_a - n_e}{N_a} \sigma_m I^{m-1} + \alpha_{fca} \right] I \quad \text{Dielectrics.} \quad (5b)$$

## 2.3 Two-temperature model

During the process of femtosecond ablation, the electron-lattice relaxation time is typically in the order of several picoseconds, while the actual laser pulse has a length of only some hundred femtoseconds, hence the material exposed to femtosecond laser pulses gets excited into a high nonequilibrium state, and the classical Fourier heat conduction equation is not applicable in such a highly nonequilibrium state. In order to solve this problem, a two-temperature model (TTM) was proposed, whose basic mechanism is sketched in fig. 2. This continuous model describes the energy transfer inside a metal with two coupled generalized heat conduction equations for the temperature of the electrons  $T_e$  and the lattice  $T_l$ :

$$\frac{\partial}{\partial t} (c_e T_e) = \nabla \cdot (k_e \nabla T_e) - G(T_e - T_l) - E_g \frac{\partial n_e}{\partial t} - \frac{\partial I}{\partial z}, \quad (6)$$

$$\frac{\partial}{\partial t} (c_l T_l) = G(T_e - T_l), \quad (7)$$

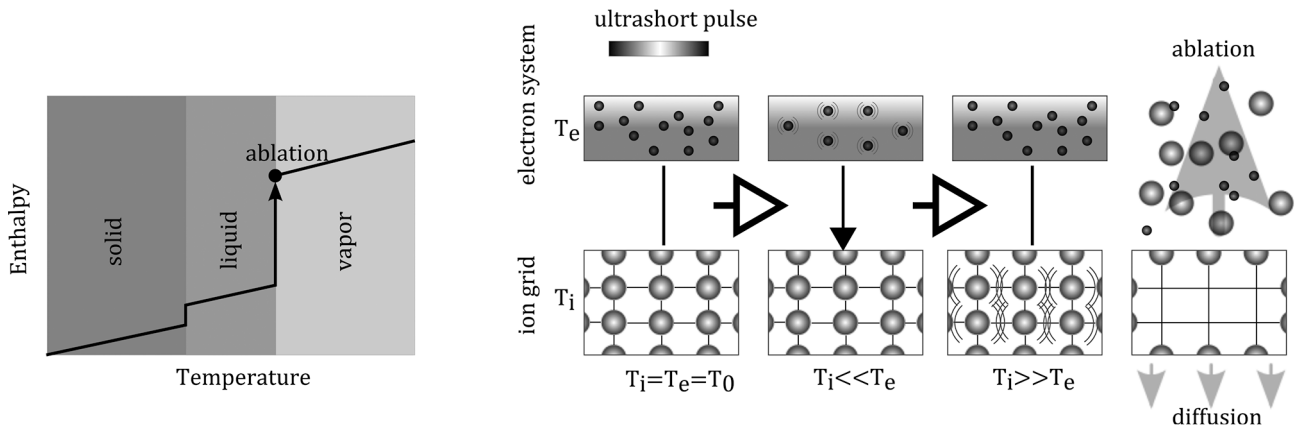


Fig. 2. Ablation models. Left: classical Fourier conduction; right: two-temperature model.

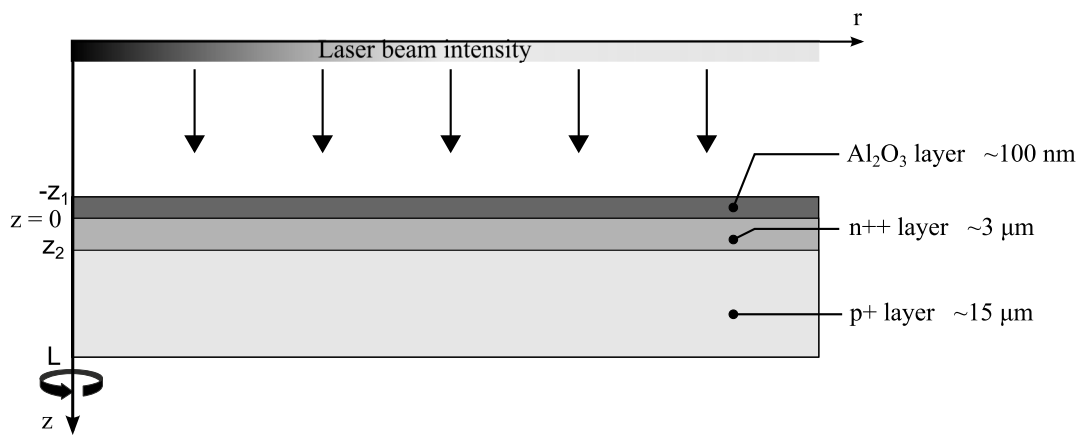


Fig. 3. Domain geometry.

where  $c_e, c_l$  are the heat capacity of the electron gas and the lattice, respectively;  $k_e$  is the electron thermal diffusivity,  $E_g$  is the energy gap of the material.  $G$  is the thermal coupling function, accounting for thermal conduction between the two systems, which is given by  $G = \frac{C_e}{\tau_r}$ , in which  $C_e$  is the free-electron heat capacity and  $\tau_r$  is the relaxation time of electrons with the lattice [7].

The last term in the right-hand side of eq. (6), the spatial derivative of  $I$  along the propagation direction, is the heat source in the equation, so that attenuation of the beam inside the material provides a positive heat source. Other terms include thermal diffusion, conduction and energy loss in overcoming the bandgap. In this model, being the energy transfer process is in the picoseconds timescale, we can neglect thermal diffusion in the lattice.

### 2.4 Geometry and boundary conditions

Given the axial symmetry of the problem it is convenient to use cylindrical coordinates  $(r, \theta, z)$  so that calculations can be restricted to two dimensions, neglecting variations of the dependent variables along the  $\theta$ -direction<sup>1</sup>. Full 3D solution is obtained revolving the solutions around the  $z$ -axis. Therefore the domain takes the simple form  $D = [0, R] \times [0, Z]$ , where  $Z = 5 \mu\text{m}$  is the total thickness of the cell and  $R = 150 \mu\text{m}$  is the radius of the disc considered for the interaction. Figure 3 contains a sketch of the geometry used in the numerical simulation, using the COMSOL suite, along with the different domain (layer) thicknesses.

The laser intensity propagates along the  $z$ -axis, normally to the layer structure of the cell. Making use of propagation matrices and given the aluminum oxide refractive index  $n_d$  and the (complex) refractive index of silicon  $n_s$  by

$$n_s = \sqrt{\epsilon}, \tag{8}$$

<sup>1</sup> This implies also that the divergence operator in (6) has to be calculated in cylindrical coordinates, namely:  $\nabla \cdot A = (\frac{\partial}{\partial r} + \frac{1}{r})A_r + \frac{\partial}{\partial z}A_z$ .

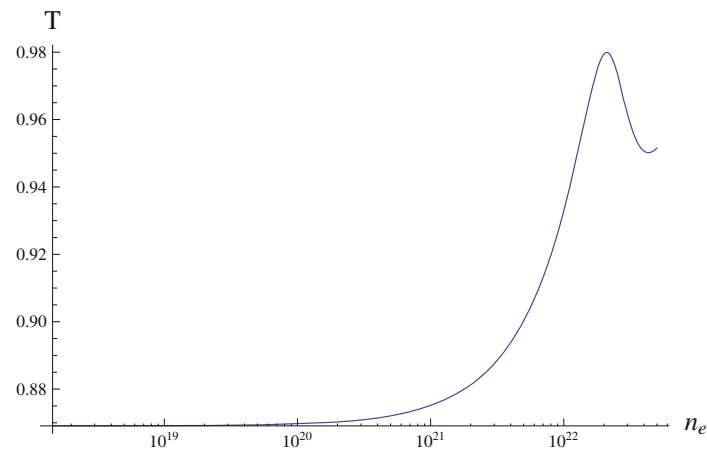


**Fig. 4.** Dielectric layer transmittance  $T$  as a function of the free electron density.

we obtain the expression for the transmission coefficient of the dielectric layer:

$$\Gamma = \frac{\tau_3 \tau_2 \exp(-i2\pi n_d L / \lambda_0)}{1 + \rho_3 \rho_2 \exp(-i2\pi n_d 2L / \lambda_0)}, \quad (9)$$

where  $L$  is the layer thickness,  $\tau$  and  $\rho$  are the elementary Fresnel transmission and reflection coefficient at normal incidence from the top sides of the interface indicated by the corresponding subscript. The transmittance of the dielectric layer is then written as

$$\mathcal{T} = \frac{\eta_0}{\text{Re}[\eta_{\text{Si}}]} |\Gamma|^2, \quad (10)$$

where  $\eta_0$  and  $\eta_{\text{Si}}$  are the vacuum and silicon characteristic impedances, respectively. Figure 4 shows that the transmittance of the dielectric layer at 800 nm is above 87% and approaches unity when the free electron density grows past  $n_{\text{cr}} (\approx 1.75 \times 10^{21} \text{ cm}^{-3})$  at 800 nm). The assumption of a lossless dielectric in the calculations is reasonable when the pulse fluence is well below the dielectric damage threshold, as is the case in the dielectric delamination process. The passivation layer then acts effectively as an AR coating, so that we can neglect reflection and assume that all the pulse energy reaches the silicon. Equivalently, under these assumptions, there is no need to solve the model equations (4b), (5b), (6), (7) in the dielectric layer. The boundary condition for the intensity at the dielectric-semiconductor interface is then simply

$$I(-z_1, r, t) = I(0, r, t) = I_0 \exp\left(-\frac{2r^2}{r_{\text{spot}}^2}\right) \exp\left(-4 \ln 2 \frac{t^2}{\tau_{\text{pulse}}^2}\right), \quad (11)$$

where  $I_0 = 2 \times 10^{12} \text{ W/cm}^2$  is the peak intensity of the pulse on the beam axis,  $r_{\text{spot}} = 50 \mu\text{m}$  is the  $1/e^2$  spot radius and  $\tau_{\text{pulse}} = 300 \text{ fs}$  is the pulse FWHM duration. This beam parameters yield a pulse mean fluence of  $F_p \sim 0.35 \text{ J/cm}^2$ . Other boundary conditions needed are heat flux conditions at the  $z = z_2$  and  $z = 0$  boundaries for the TTM equations (6), (7). Given the timescale of the problem, only radiation loss through the  $z = 0$  plane should be taken into account, anyway the effect is negligible so that the insulation of boundary conditions gives the same results.

## 2.5 Numerical calculation

The set of eqs. (4)–(7), (11) has been solved with COMSOL, a finite element software, in the geometry described above. A good meshing is achieved with a  $30 \times 25$  grid on the  $z$ - $r$  plane, with smaller size near the target surface. The 3D elements are then obtained naturally revolving the two-dimensional mesh around the  $r = 0$  axis. Results from the simulation are presented in figs. 5 and 7. The scale of the  $z$ -axis has been expanded to better observe the solution features. In the early stages of the pulse the unexcited material shows essentially linear absorption, with the pulse intensity decaying exponentially inside the medium. When the electron density approaches the critical density, the absorption grows almost exponentially with the electron density, leading to the deposition of the laser energy in the first hundred of nanometers. This in turn confines the free electron growth in the same layer near the surface, reaching a plasma state.

The electron temperature grows rapidly during the pulse reaching a peak temperature in the order of 7.9 eV about 300 fs after the pulse peak. The average ionization is around 2, which is consistent with the calculations made in [12]

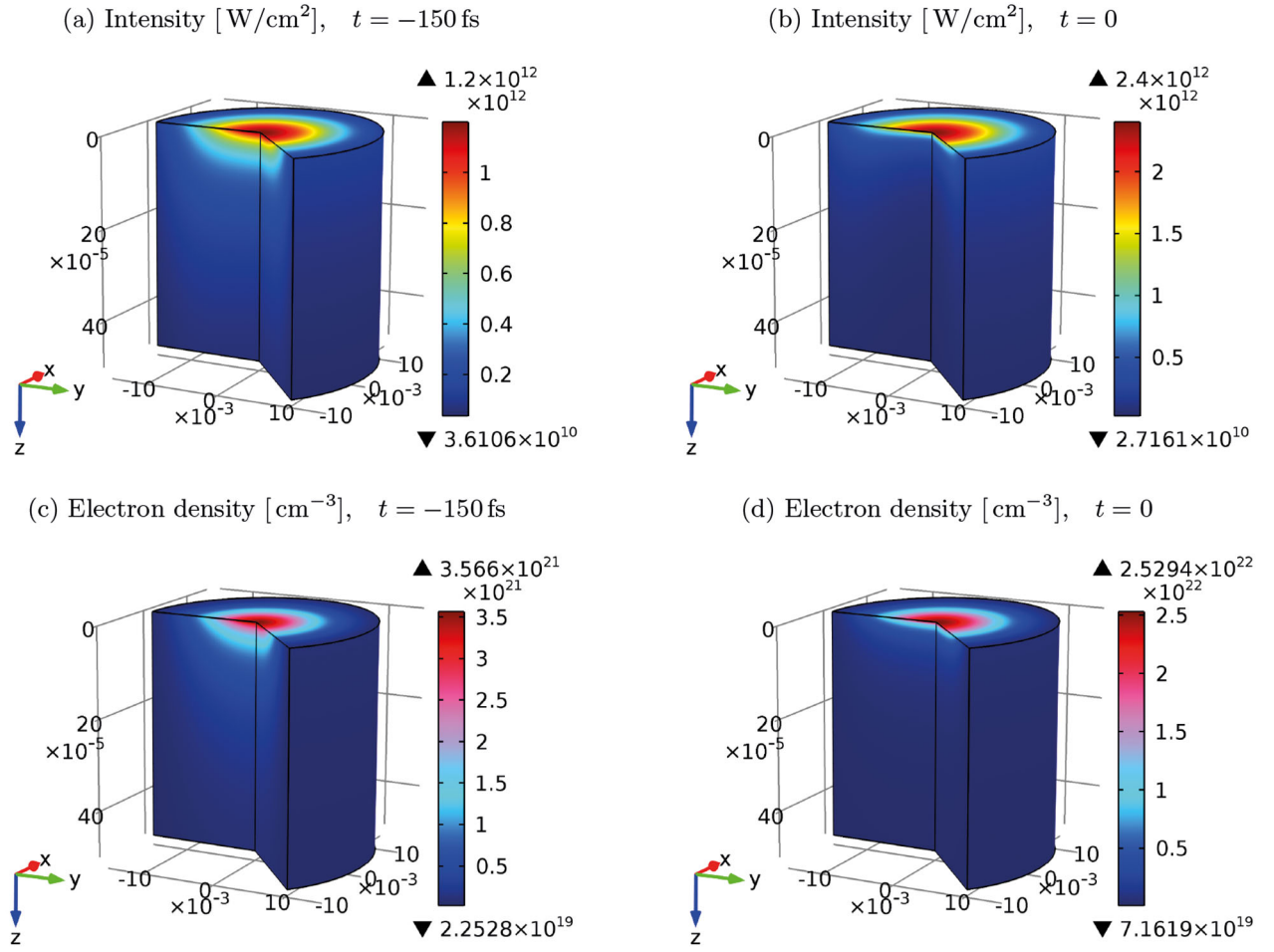


**Fig. 5.** Electron density and intensity profiles inside the target. Time is referred to the pulse peak. Note that different axis scales are used for the transverse and longitudinal dimensions in order to visualize the superficial heating phenomena, that would be unreadable with equal scales.

for the estimate of the average ion charge and electron temperature through the Saha equation. We can calculate the number of particle in the Debye sphere as [13]

$$N_D = 1.7 \times 10^9 \sqrt{T_e^3/n_e}, \quad (12)$$

which gives in our case  $N_D < 1$ . This means that the electron plasma is highly nonideal, because under these conditions the energy of Coulomb interactions is stronger than the thermal energy of the particles. In addition, it is noteworthy to compare the calculated electron temperature with the Fermi degeneracy temperature for the corresponding electron gas, given by [11]

$$\epsilon_f = \frac{\hbar^2}{2m_e} (6\pi^2 n_e)^{2/3} \approx 7.8 \text{ eV}. \quad (13)$$

This comparison points out that electrons in our model behave as an interacting and degenerate Fermi gas [14]. Making use of the electronic density of states in the conduction band in silicon

$$\delta_c = \frac{2m_e^{3/2}}{2\pi^2 \hbar^3} \sqrt{E - E_f},$$

we can estimate a quasi-Fermi level for electrons in the semiconductor of  $\sim 1$  eV. Because the quasi-Fermi level is close to the conduction band, the full Fermi-Dirac (FD) distribution should be used, which is also evident comparing the Boltzmann and FD distribution functions  $f[E]$  for the electron gas in fig. 6, clearly there are significant differences right above the conduction band of silicon (1.12 eV).

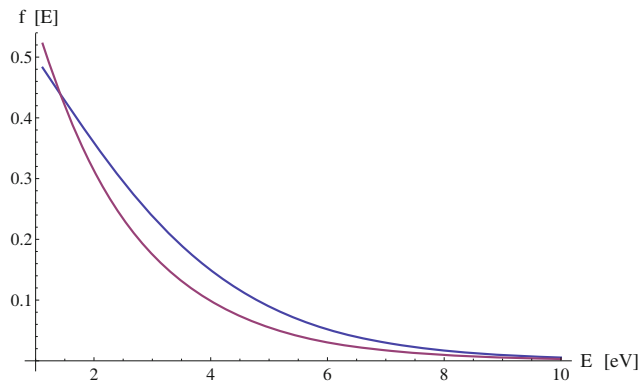


**Fig. 6.** Occupancy probability distribution for the electron gas in silicon: FD (blue line) and Boltzmann (purple line). The  $x$ -axis origin is taken as the conduction band energy.

Even though one should take into account the modifications to the thermodynamic functions due to Coulomb interactions in the gas, there are no analytical expressions for a nonideal Fermi gas and for the scope of this simplified model we will neglect the contribution from collisions. The heat capacity of the electron gas  $C_e$ , for temperatures much smaller than the Fermi temperature, can then be expressed as [14, 15]

$$\frac{C_e}{n_e k_b} = \frac{\pi^2}{2} \frac{k_b T_e}{\epsilon_f}. \quad (14)$$

Using the heat capacity of an ideal gas in eq. (6), which is correct in the high fluence regime when the electron temperature grows past the Fermi temperature, would result in an overestimate for the heat capacity during the initial electron heating, resulting in a lower electron temperature at the end of the pulse. However, the effect is not critical because lower heat capacity leads to faster electron heating which in turn, because of the linear dependence for low temperatures of the heat capacity to the temperature, makes the heat capacity quickly approach the classical limit. To address the problem of which statistic has to be used, we first calculate the solutions for the ideal gas statistics and make use of the fugacity  $\bar{R}$  of the electron gas. Being  $\lambda_{th} = h/(2\pi m_e k_b T_e)^{1/2}$  the electron thermal wavelength and  $v = \sqrt[3]{1/n_e}$  the average interparticle distance, the fugacity can be written as  $\bar{R} = n_e \lambda_{th}^3 = (\lambda_{th}/v)^3 \ll 1$ . Carrying the calculation of the fugacity over the solutions of the problem shows that, while being  $\bar{R} = 10^{-4}$  in any point of the domain during the simulation,  $\bar{R}$  is not small enough to allow the use of the Fermi statistics in the limit  $\bar{R} \rightarrow 0$ . This fact is also confirmed by the fact that the electron temperature is close to the Fermi degeneracy temperature. In this intermediate regime we make use of the virial expansion to calculate the departure of the gas from classical due to quantum effects [14]:

$$C_e \simeq \frac{3}{2} \left[ 1 - 0.0884 \left( \frac{\lambda_{th}^3}{v} \right) + 0.0066 \left( \frac{\lambda_{th}^3}{v} \right)^2 + \dots \right]. \quad (15)$$

Under the conditions of the problem the deviation from the classical analysis is negligible because the expression given in (15) gives a correction to the electron heat capacity of less than one part per million, so that, under the simplifying assumptions already made, Boltzmann statistics suffices for our treatment. It takes about 4 ps for the electrons to release most part of their energy to the lattice and after 10 ps electrons and ions reach thermal equilibrium (figs. 7(d), 7(b)). It is interesting to notice that the peak temperature of the ions is reached inside the material rather than on the surface. This is because the electron-ion scattering process starts to be slowed down by Coulomb screening over critical electron densities [16], so that the heat exchange is more efficient in regions far from the surface, where the ionization degree is lower.

## 2.6 Results discussion

As seen already in previous works [17, 18] in molecular dynamics (MD) simulations, what characterizes the ultrafast interaction is the initial isochoric heating of the material up to a supercritical fluid, which then relaxates following different paths in the phase diagram while the material expands quasi-adiabatically. Each path distinguishes among the different mechanisms involved in the ablation process and each one is associated with a different energy density absorbed. The material is heated to a temperature close to the critical temperature of silicon and is then pushed into the metastable region between the spinodal and binodal lines, causing homogeneous nucleation of gas bubbles in the

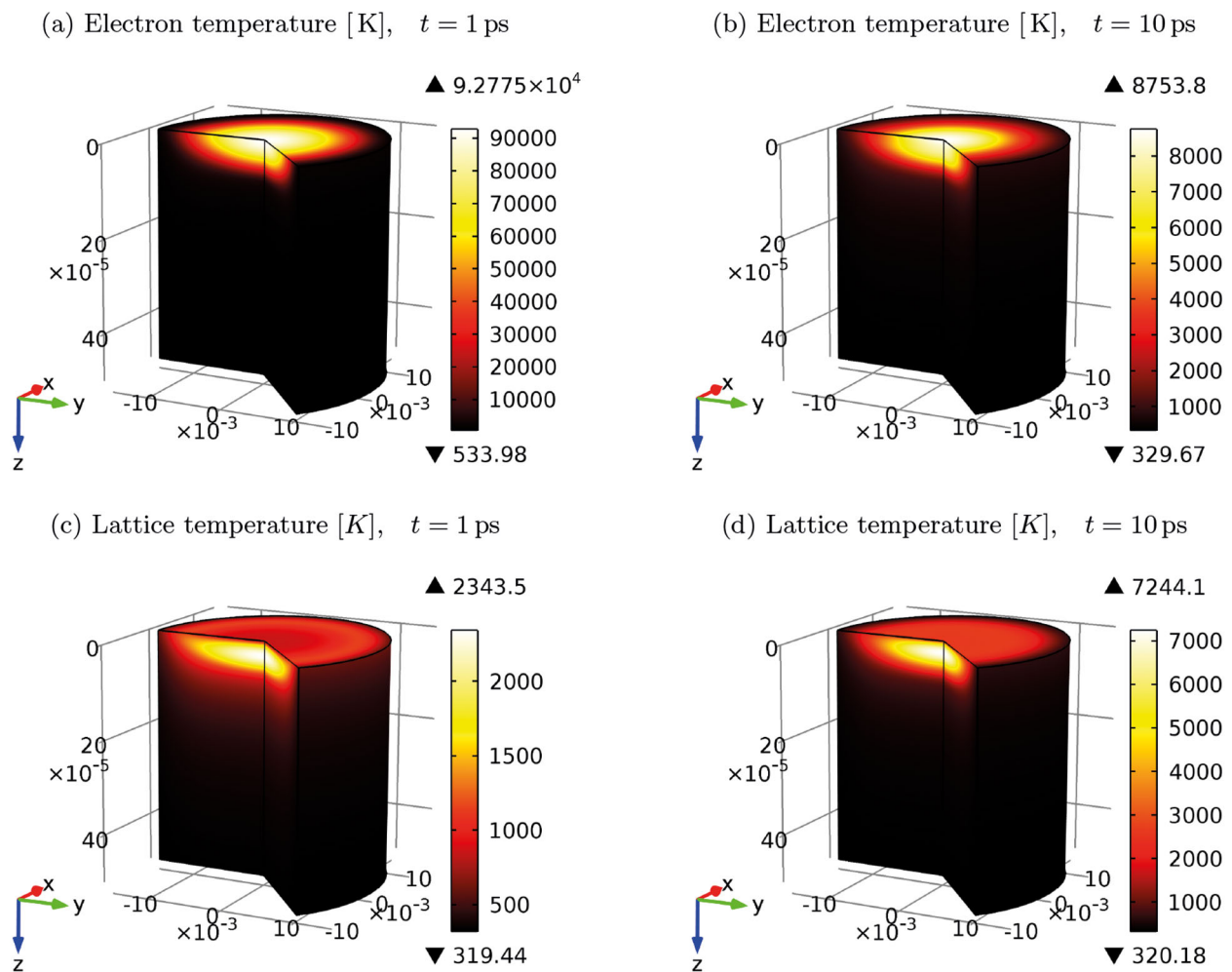


**Fig. 7.** Electron and lattice temperature distributions inside the target. Time is referred to the pulse peak.

superheated liquid, a mechanism which goes under the name of phase explosion. After the initial constant volume heating a superheated and highly pressurized liquid layer forms near the surface. The time for electrons to thermally diffuse out of the interaction volume is considerably longer than the time it takes for electrons to transfer their energy to ions, so that a strong compressive shock wave emerges, driven by the strong pressure discontinuity. A rough estimate of the initial pressure can be made with the ideal gas equation of state and Boltzmann distribution. A particle density of  $3 \times 10^{22} \text{ cm}^{-3}$  with a temperature of 92000 K yield  $\sim 36$  GPa. This pressure is confrontable with the Young modulus of most solids (150 GPa for silicon and 353 GPa for aluminum oxide).

The resulting delamination follows as a result of spallation: the shock front, after transmission into the oxide layer, is reflected from the free surface, transforming into a tensile wave which tends to accelerate the layer into vacuum, causing detachment when the resulting stress exceeds the interface strength [19].

This effect is relevant in the silicon solar cell manufacturing as the control of the ablation is crucial in the control of the opening of contacts [3]. Moreover, the advent of high-average-power ytterbium femtosecond mode-locking lasers have provided the tool for the exploitation of the ablation mechanism described in this model with processed areas that are relevant for industrial processes.

The comparison of the experiments in this novel process regime with the theoretical and modeling predictions as these here proposed is under way in a number of Laboratories including ours.

This work has been funded by the Polo Fotovoltaico Veneto (SMUPR n. 4148 “Polo di ricerca nel settore Fotovoltaico” POR CRO PARTE FESR 2007-2013 Azione 1.1.1 a regia Regionale), and carried out at the Laser4PV Labs of Polo Fotovoltaico Veneto, Università di Padova.

## References

1. Armin G. Aberle, Wu Zhang, Bram Hoex, Energy Proc. **8**, 244 (2011).
2. Tino Rublack, Gerhard Seifert, Opt. Mater. Express **1**, 543 (2011).
3. M. Zanucoli, *et al.*, *Numerical simulation and modeling of rear point contact solar cells*, in *IEEE 37th Photovoltaic Specialists Conference (PVSC), 2011* (IEEE, 2011).
4. S. Buratin, P. Villoresi, Opt. Mater. Express **3**, 1925 (2013).
5. M.I. Kaganov, I.M. Lifshitz, L.V. Tanatarov, Sov. Phys. JETP **4**, 173 (1957).
6. T.Q. Qiu, C.L. Tien, J. Heat Transfer **115**, 835 (1993).
7. Benxin Wu, Yung C. Shin, Appl. Surf. Sci. **255**, 4996 (2009).
8. Nadezhda M. Bulgakova *et al.*, Appl. Phys. A **81**, 345 (2005).
9. B.C. Stuart *et al.*, Phys. Rev. B **53**, 1749 (1996).
10. Henry M. Van Driel, Phys. Rev. B **35**, 8166 (1987).
11. Ya.B. Zel'Dovich, *Physics of Shock Waves and High-Temperature Hydrodynamic Phenomena* (Academic Press, New York, London, 1966).
12. Eugene G. Gamaly *et al.*, Phys. Rev. B **73**, 4101 (2006).
13. F.F. Chen, *Introduction to Plasma Physics and Controlled Fusion* (Springer, 1984).
14. R.K. Pathria, P.D. Beale, *Statistical Mechanics* (Elsevier, 2011).
15. K. Huang, *Statistical Mechanics* (Wiley, New York, 1987).
16. T. Sjodin, H. Petek, H.L. Dai, Phys. Rev. Lett. **81**, 5664 (1998).
17. Delphine Bouilly, Danny Perez, Laurent J. Lewis, Phys. Rev. B **76**, 184119 (2007).
18. Patrick Lorazo, Laurent J. Lewis, Michel Meunier, Phys. Rev. Lett. **91**, 225502 (2003).
19. L. Davison, *Fundamentals of Shock Wave Propagation in Solids* (Springer-Verlag, Berlin, 2008).